The Astrophysical Journal Supplement Series, 250:19 (14pp), 2020 September https://doi.org/10.3847/1538-4365/abaa4d

Panning for Gold: New Emission Lines from UV–VIS Spectroscopy of Au I and Au II

S. J. Bromley[1], C. A. Johnson[2], D. A. Ennis[2], G. J. Hartwell[2], D. A. Maurer[2], S. D. Loch[2], P. C. Stancil[3], B. M. McLaughlin[4], C. E. Sosolik[1], and J. P. Marler[1]
[1] Department of Physics and Astronomy, Clemson University, Clemson, SC 29631, USA; sjbroml@clemson.edu
[2] Department of Physics, Auburn University, Auburn, AL 36849, USA
[3] Department of Physics and Astronomy and Center for Simulational Physics, University of Georgia, Athens, GA 30602, USA
[4] Centre for Theoretical Atomic, Molecular, and Optical Physics, School of Mathematics & Physics, Queen's University of Belfast, Belfast, BT7 1NN, Northern Ireland, UK
Received 2020 April 17; revised 2020 July 6; accepted 2020 July 28; published 2020 September 10

Abstract

The recent detection of a neutron star merger by the LIGO collaboration has renewed interest in laboratory studies of *r*-process elements. Accurate modeling and interpretation of the electromagnetic transients following the mergers requires computationally expensive calculations of both the structure and opacity of all trans-iron elements. To date, the necessary atomic data to benchmark structure codes are incomplete or, in some cases, absent entirely. Within the available laboratory studies, the literature on Au I and Au II provides incomplete reports of the emission lines and level structures. We present a new study of Au I and Au II lines and levels by exposing a solid gold target to plasma in the Compact Toroidal Hybrid (CTH) experiment at Auburn University. A wavelength range from 187 to 800 nm was studied. In Au I, 86 lines are observed, 43 of which are unreported in the literature, and the energies of 18 $5d^9 6s6p$ levels and 16 of the 18 known $5d^9 6s6d$ levels are corroborated by a least-squares level energy optimization. In Au II, 76 emission lines are observed, and 51 of the lines are unreported in the literature. For both Au I and Au II, the new lines predominantly originate from the most energetic of the known levels, and over half of the new Au II lines have wavelengths longer than 300 nm. For the estimated electron parameters of CTH plasmas at the gold target ($n_e \sim 10^{12}$ cm^{-3}, $T_e \sim 10$ eV), two-electron transitions are similar in intensity to LS-allowed one-electron transitions.

Unified Astronomy Thesaurus concepts: Atomic spectroscopy (2099); Laboratory astrophysics (2004); Spectral line lists (2082); Spectral line identification (2073); R-process (1324); Chemically peculiar stars (226)

1. Introduction

The production of elements up to iron within stars has been studied for many years and is well understood (Liccardo et al. 2018). Absorption from heavier elements such as gold, platinum, and osmium has been observed in a number of stars (Jaschek & Malaroda 1970; Guthrie 1984; Fuhrmann 1989; Castelli et al. 2017). A large portion of these heavy elements ($Z \gtrapprox 54$) are produced solely from *r*-process nucleosynthesis (Kajino et al. 2019). The conditions for their production are primarily found in either core-collapse supernovae or neutron star mergers (NSMs; Côté et al. 2018; Kajino et al. 2019). With the detection of the NSM GW170817 (Abbott et al. 2017) and its electromagnetic counterparts, e.g., Coulter et al. (2017) or Margutti et al. (2017), direct spectroscopic studies of active *r*-process nucleosynthesis are possible. To date, the exact structure and composition of the ejecta remains an open question, and the spectra contain no sharp features that could enable the identification of individual elements. However, the color evolution of the electromagnetic transient suggests radioactive heating caused by 0.01–0.05 $M_\odot$[5] of *r*-process-rich material (Drout et al. 2017).

Analysis of NSM spectra is further complicated by the presence of two or more possible ejecta components (see Kasen et al. 2017 or Kawaguchi et al. 2018 and references therein), including the dynamical *r*-process-rich ("red") component. Extracting *r*-process abundances from the broad spectra of GW170817 is a difficult task and requires rigorous calculations of the ejecta opacity, e.g., the calculations by Kasen et al. (2013) and Fontes et al. (2020). In the dynamical ejecta, heavy elements—for example, the lanthanides with open *f* shells—dominate this opacity, and the relative contribution of these elements is orders of magnitude larger than iron-rich material (Kasen et al. 2013). Proper treatment of the opacity requires calculations of the atomic structure for the neutral through doubly ionized stages of each element. For most elements heavier than iron, the available atomic data are far from complete and in most cases lacking measurements or robust calculations.

The effect of accurate (experimental) atomic data on the opacity calculations and the resulting NSM *r*-process abundances has yet to be determined. Even in the absence of appropriate benchmarks, structure calculations for such heavy elements involve core–valence coupling, core polarization, significant configuration interaction, and relativistic effects (Quinet 2017). As discussed in Kramida (2019), the atomic structure codes currently available are not sufficient for accurately reproducing the measured spectra of heavy elements. There is a clear need to study the spectra of these astrophysically relevant species. New experimental measurements of the lines and levels of these high-*Z* elements will be beneficial for interpretations of future NSM spectra, *r*-process abundance studies of stellar atmospheres, and benchmarks for atomic structure calculations.

Among the high-*Z* elements expected in NSM ejecta, neutral and singly ionized gold are two of the relatively simpler systems. The ground state of neutral gold (Au I) consists of a closed $5d$ shell with a single valence $6s$ electron, and excited states of the system commonly take the form $5d^{10}nl$ or

[5] $1\ M_\odot = 1.98 \times 10^{30}$ kg.

$5d^9(^2D)6snl$, where the outer electrons ($6snl$) couple together before coupling to the core (Ehrhardt & Davis 1971). In singly ionized gold (Au II), the configuration interaction is significant, and the coupling between the $5d^9$ or $5d^8$ cores and the valence shells leads to a large number of levels.

The bulk of the known emission lines for Au I and Au II come from the surveys of hollow cathode spectra by Platt & Sawyer (1941, hereafter PS), Ehrhardt & Davis (1971, hereafter ED), and Rosberg & Wyart (1997, hereafter RW). Platt & Sawyer primarily focused on Au I, and the work of Ehrhardt & Davis corroborated the level structures from the former. For both Au I and Au II, many of the emission lines observed by one of the surveys are absent from the spectra of the other two. For example, lines from the Au I $5d^96s6p(^4D_{5/2})$ level of Platt & Sawyer are absent from the spectra of Ehrhardt & Davis. However, ED's spectra contained few lines from levels with large orbital angular momentum, and excitation of levels with a $5d^9$ core was generally lacking. To date, levels of the $5d^96s6p$ and $5d^96s6d$ configurations of Au I have yet to be corroborated by multiple sources.

The Au II literature contains similar problems, and both PS and ED reported significantly fewer lines in Au II compared to Au I. However, Rosberg & Wyart (1997) saw significant excitation of Au II in a hollow cathode, from which they classified over 400 lines and reported $\log(gf)$ values from a Cowans code structure calculation; of their 400+ transitions, less than 30 have wavelengths longer than 300 nm. To date, the electronic structure of Au II remains incomplete, and levels between 135,000 cm^{-1} and the ionization limit at 162,950 cm^{-1} have yet to be reported. These levels likely belong to the triply excited configurations, e.g., $5d^76s^26p$, and have yet to be investigated aside from a single level in Rosberg & Wyart (1997). Even so, many of the known levels below 135,000 cm^{-1} have few to no reported visible transitions associated with them.

All three surveys (PS, ED, and RW) utilized hollow cathode sources wherein the high electron densities are often offset by a lower electron temperature. Though ED also studied arc and spark spectra, the measurements are limited to the range 300–400 nm. Comparing the three studies, it is apparent that the population of the higher energy levels was generally low or similar, as many of the corresponding transitions have very low intensities. It can be expected that a plasma source with a higher electron temperature may yield significant excitation of these levels, and new transitions from these levels may be observed. New ultraviolet–visible (UV–VIS) measurements of Au I and Au II, when combined with the previous surveys, could provide relatively complete spectra for benchmarking future atomic structure calculations of these systems.

A new systematic study of the emission lines and corresponding energy levels of the Au I and Au II systems between 187 and 800 nm is presented. In Section 2.1, the experimental setup utilizing the Compact Toroidal Hybrid (CTH) is described, which provides a combination of electron temperatures and densities not achieved by previous experimental studies of gold. Analysis of the observed spectra is discussed in Section 2.2 and the findings for Au I and Au II are presented in Section 3. In Section 4, the conclusions of the work are discussed.

2. Experimental Program

2.1. Measurements

Spectral measurements of gold emission were acquired using the CTH plasma experiment at Auburn University (Hartwell et al. 2017). The CTH is a stellarator/tokamak hybrid device developed to investigate the effects of 3D magnetic shaping on the stability of current-carrying plasmas. While the CTH is capable of operating without driving plasma currents, this work utilizes current-carrying discharges similar to previous experiments that investigated potential plasma diagnostic lines of W I (Johnson et al. 2019b). Current-carrying discharges presented in Section 3 evolve over 50–80 ms with peak plasma currents of 60–68 kA in the region of the Au emission.

Gold-tipped probes are inserted into CTH plasmas, and UV-optimized collection optics couple emission from the plasma–probe interaction region to a Princeton Instruments HRS 500 spectrometer equipped with a 1200 line mm^{-1} grating (Johnson et al. 2019b). Gold probe tips were fabricated by electroplating $0\farcs75 \times 1\farcs0$ nonmagnetic steel cylinders with a thin nickel layer followed by a 4 μm layer of pure gold. During a CTH plasma discharge, gold is eroded from the surface of the probe tip, excited, and ionized. Emission from eroded gold atoms is captured by 1.25 ms spectral exposures throughout the discharge. To aid in identifying lines arising from the nickel layer and underlying steel, spectra were collected from a third SS plug coated in 25 μm of pure nickel.

In total, 127 discharges were diagnosed with three probe tips (two gold, one nickel) at depths of 0, 3, 6, and 9 cm relative to the edge of the plasma. The spectrometer grating position associated with each plasma discharge captures a spectral bandwidth corresponding to ~40 nm. The range from 187 to 800 nm was compiled using 17 different grating angles such that the neighboring wavelength windows had a 2–3 nm overlap.

2.2. Data Analysis

Over 5000 individual spectra were collected from discharges with the three different probe tips. Spectral features resulting from the contamination of X-rays striking the spectrometer charge-coupled device are identified by their transitory nature and wavelength localization. The X-rays are filtered from the spectra by interpolating affected pixels between their two neighboring, clean pixels. A sample spectra showing the raw versus X-ray-filtered data is presented in Figure 1.

Each peak in the spectrum is identified, and the central wavelength is determined from a Gaussian fit. Statistical uncertainties are taken as the standard deviation of each peak's central wavelength across all exposures and are on order 0.02 nm. The spectrometer was wavelength-calibrated using IntelliCal software from Princeton Instruments and an Hg lamp.

A sample of the identified background lines across many wavelength windows is shown in Table 1. For most of the spectra, the measured wavelength uncertainty is less than 0.02 nm. The largest discrepancy (0.05 nm) is observed for the $n = 3 \rightarrow 2$ transition in H I but appears to be an outlier. Nevertheless, as an upper bound, a wavelength uncertainty of 0.05 nm is adopted for all of the observed wavelengths in the following sections. The total uncertainty is then taken as the quadrature sum of the statistical uncertainty (~0.02 nm) and the estimated systematic uncertainty (0.05 nm).

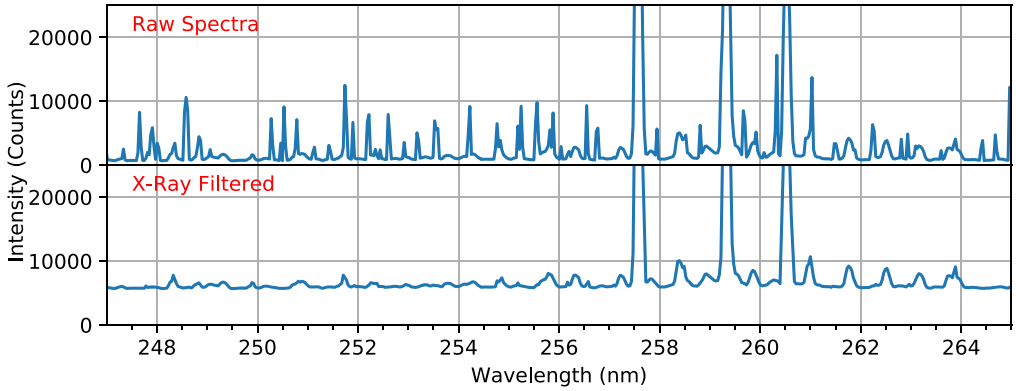

Figure 1. Raw spectral measurement from a 1.25 ms exposure (shot number 18113011, exposure 112) with the gold probe inserted 6 cm inside the edge of the plasma during the current-carrying portion of the discharge (top) and the spectral data processed by the software X-ray filter (bottom).

Table 1
Comparison of Some Observed Contaminant Lines vs. Their Wavelengths in the NIST Database (Kramida et al. 2020)

Source	$\lambda_{\rm NIST}$ (nm)	$\lambda_{\rm obs}$ (nm)	$\Delta\lambda$ (nm)
C III	229.69	229.68(02)	0.01
C III	279.45	279.46(01)	−0.01
Fe II	279.79	279.77(02)	0.02
Fe II	294.84	294.84(03)	0.0
O III	326.55	326.54(01)	0.01
Fe I	359.27	359.27(02)	0.0
H I	434.05	434.05(01)	0.0
N II	472.16	472.16(02)	0.0
H I	486.14	486.14(0)	0.0
C I	588.95	588.96(0)	−0.01
C I	601.65	601.63(01)	0.02
N I	648.17	648.17(01)	0.0
H I	656.27	656.22(0)	0.05
Fe I	685.52	685.50(01)	0.02
N I	746.83	746.85(01)	−0.02
C III	778.04	778.03(0)	0.01

Note. Experimental uncertainties are listed in parentheses. All wavelengths shown are reported in air.

In the wavelength range between 187 and 800 nm, there are thousands of possible E1 transitions from both Fe I and Fe II. In many cases, transitions matching the level structure of gold overlap with Fe lines that are present in both the gold and nickel spectra. The spectra also contain many lines from background gases and other plasma-facing materials (Cr, Ni) that can change quite dramatically with time. For example, Figure 2 shows the time dependence of the 486 nm Balmer line of neutral hydrogen through a single discharge. As H is the working gas, the line is present in both the current-free ($t < 70$ ms) and current-driven ($t > 70$ ms) portions.

Figure 3 shows a similar plot for a strong transition in Au I. As shown, the intensity of the Au I spectral lines increases with probe tip depth, and the Au I emission line is entirely absent from the nickel spectra. Depending on the upper level, we find that lines belonging to the most highly excited levels are generally only present during the current-driven portion of the discharge. Though many suspected Au lines follow a similar trend as in Figure 3, a good number are contaminated by possible overlapping transitions in Fe, Cr, or background gases. By comparing the nickel and gold spectra for similar plasma conditions, a list of gold candidate lines can be generated.

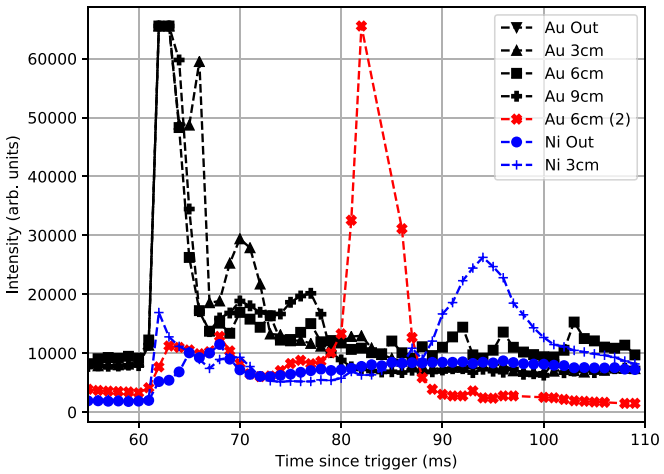

Figure 2. Time dependence of the 486 nm H I line (CTH shot numbers in descending legend order: 18112724, 18112745, 18112759, 18112765, 18113017, 18112910, 18112922). The spectral line height is plotted as a function of time for the first gold probe at insertion depths of 0 (downward triangles), 3 (upward triangles), 6 (squares), and 9 (thick black plus signs) cm. Line heights from the second gold probe at 6 cm insertion (red crosses) and the nickel probe at 0 (blue circles) and 3 (thin blue plus signs) cm are shown. Data are shown for both the current-free ($t < 70$ ms) and current-driven ($t > 70$ ms) portions.

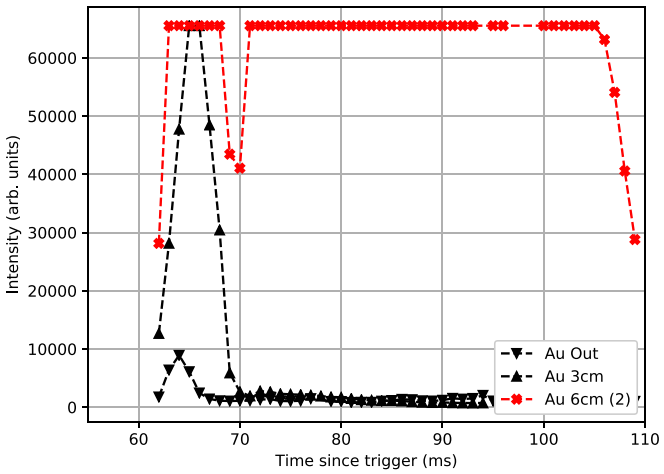

Figure 3. Time dependence of the intense 267.54 nm Au I line. The spectral line height is plotted as a function of time for the first gold probe tip at an insertion depth of 0 (downward triangles; shot 18112718) and 3 (upward triangles; shot 18112739) cm and a second gold probe tip at an insertion depth of 6 cm (red crosses; shot 18113008). The emission at 267.54 nm is below the noise floor when the nickel probe tip was inserted.

To narrow the gold candidate list and identify new lines of Au I and Au II, we adopted the following procedure. A list of all possible allowed E1 transitions ($\Delta J = 0, \pm 1$ and changes in parity) was generated from the known levels in the literature. We note that in Au I and Au II, the spin–orbit coupling is not insignificant, and constraints on L and S, $\Delta L = 0, \pm 1$ and $\Delta S = 0$, may not be reliable (Ehrhardt & Davis 1971). This is illustrated by transitions between levels with different core configurations, such as $5d^{10}5f\ (^2F^{\circ}_{5/2}) \rightarrow 5d^9 6s^2\ (^2D_{3/2})$ of Au I at 217.08 nm (Platt & Sawyer 1941).

The list of calculated Ritz wavelengths is converted from vacuum to air wavelengths with the IAU standard conversion from Morton (2000). The list of air wavelengths is compared to the list of peaks in the spectra, and matches are restricted to within the typical uncertainty of the observed wavelengths, i.e., $|\lambda_{\rm obs.} - \lambda_{\rm ritz}| < 0.06$ nm. To confirm the assignment of energy levels to each transition, the match list was used to perform a least-squares level energy optimization with the code "LOPT" (Kramida 2011). Only lines whose behavior strongly indicates a gold transition were used. As the spectra are lower resolution than the previous work in the literature, the optimization is used to aid the identification of new lines and check for consistency against the available literature. In the level optimization, lines that have large discrepancies with the Ritz wavelengths, as calculated from the optimized level energies, were removed from consideration. Where necessary, level energies were fixed with respect to the ground state to improve the agreement between the optimized energies, Ritz wavelengths, and available literature. The details regarding the final choice of fixed levels and their effects on the relevant quantities are discussed in Section 3.

When pointing the fiber to the sides of the probes, a significant decrease in the counts of known Au I lines was observed, indicating that most of the emission from the eroded material is close to the probe surface. At the probe surface, the plasma conditions are estimated by modeling Fe II emission with the collisional-radiative code ColRadPy (Johnson et al. 2019a). As the uncertainty of the underlying Fe II atomic data is unknown, we estimate the uncertainty in our Fe II model at ±20% for both electron density and temperature. Our best agreement between observed and synthetic spectra results from T_e of order 10 eV and n_e of order 10^{12} cm^{-3} at the probe tip. These numbers are similar to those found in the previous study of W I by Johnson et al. (2019b).

The calculation of the reported intensities needs to consider two aspects: (1) each discharge develops in time in a similar but not identical manner, and (2) the instrument response, as a function of wavelength, is not known. To item (1), we chose to report line intensities from the same single time in 17 different discharges where the plasma conditions are most similar. In the choice of exposures, the central densities are, on average, $n_e = (1.0 \pm 0.5) \times 10^{13}$ cm^{-3}, and the plasma currents are 59 ± 6 kA. At the location of the probe, the conditions are similar to those quoted previously ($n_e \sim 10^{12}$ cm^{-3}, $T_e \sim 10$ eV).

For item (2), no external calibration source was available. Therefore, we have modified the relative intensity calibration procedure from Whaling et al. (1993), where argon branching fractions were employed to compare spectra on the same (relative) intensity scale. Consider two transitions from the same upper level with wavelengths λ_1 and λ_2. If the A values are known, the branching fraction may be written

$$\mathrm{BR}_{1,2} = \frac{A_1}{A_2} = \frac{I_1/\epsilon(\lambda_1)}{I_2/\epsilon(\lambda_2)}, \tag{1}$$

where the intensities I_1 and I_2 are found by integrating over the spatial extent of the peaks, and the photon detection efficiencies ϵ are functions of wavelength (Whaling et al. 1993). If several such transitions from the same upper level with known branching fractions are observed, the photon detection efficiencies $\epsilon(\lambda)$ can be calculated and used to place the overlapping spectra on the same relative intensity scale. In our spectra, the observed transitions of Fe I, Fe II, and background gases are insufficient for performing the procedure outlined by Whaling et al. (1993).

Using the integrated heights of peaks within the spectral overlap of neighboring discharges, the present intensity calibration is adapted from Whaling et al. (1993). Consider two discharges, labeled i and $i + 1$, with a several nm overlap in wavelength coverage. At a time where the plasma conditions (electron density, plasma current) are similar, the change in peak heights may be attributed to the change in instrument response between the two grating positions. The conversion factor for intensities in range $i + 1$ to the scale of range i may be calculated by

$$S_{i,i+1} = \frac{1}{N}\sum_{j=1}^{N} \frac{I_j^{(i+1)}}{I_j^{(i)}}, \tag{2}$$

where the sum is over the number of peaks N within the overlap region, and the intensities $I^{(i)}$ and $I^{(i+1)}$ are calculated by numerical integration of a Gaussian fit to each peak in the respective wavelength regions. The factor $S_{i,i+1}$, when expanded across all wavelengths, mimics the photon detection efficiency $\epsilon(\lambda)$ in Equation (1). For the 16 overlap regions, between one and 11 peaks (four on average) were used to place the entire 187–800 nm wavelength range on the same intensity scale using Equation (2). This procedure provides intensity scaling factors at the overlap wavelengths. The values between these small overlap regions are calculated by linear interpolation, and the edge cases are considered as follows. In the first wavelength range, the conversion factor is interpolated from 0% efficiency at the UV cutoff in air (∼187 nm) to the efficiency at the first overlap region (227 nm). The last overlap region at 767 nm contains no peaks, and the values in the final wavelength window are extrapolated from the previous region.

The validity of the postcorrection intensities may be checked with known branching ratios, the intensity response S substituted for $\epsilon(\lambda)$, and integrated intensities with Equation (2). Only one pair of the observed Au I transitions shares the same upper level and has previously reported A values: the 242.79 and 312.28 nm transitions from $5d^{10}6p\ (^2P^{\circ}_{3/2})$. Both transitions are possibly blended with transitions from Au II and a nearby transition of Fe II. At the time specified above, calculation of the ratio $I(243)/I(312) = 5$ is unaffected by the intensity calibration. Despite the ratio being an underestimate due to saturation of the peak at 242.79 nm, the ratio is within a factor of ∼2 of the known value (10.4; Kramida et al. 2020).

As an additional check on this procedure, we identified Fe I and Fe II lines in our spectra for which A values are available in the National Institute of Standards and Technology (NIST)

Table 2
Observed Transitions in Au I

Rel. Intens.	$\lambda_{obs.}$	λ_{Ritz}	$\Delta\lambda$	Lower Level	J_l	Upper Level	J_u	Note	References
0	201.26(06)	201.22(02)	0.04	$5d^9 6s^2\ ^2$D	5/2	$5d^9 6s6p\ ^2$P°	3/2		PS
0	212.68(05)	212.67(03)	0.01	$5d^{10} 6s\ ^2$S	1/2	$5d^9 6s6p\ ^4$P°	3/2		PS
1	217.09(05)	217.09(05)	0.0	$5d^9 6s^2\ ^2$D	3/2	$5d^{10} 5f\ ^2$F°	5/2	Broad	PS
0	229.11(06)	229.07(02)	0.04	$5d^9 6s^2\ ^2$D	5/2	$5d^9 6s6p\ ^2$F°	7/2	Bl. (Fe II)	New
1	235.24(05)	235.27(02)	−0.03	$5d^9 6s^2\ ^2$D	5/2	$5d^9 6s6p\ ^2$D°	5/2	Bl. (Fe II)	PS
0	236.17(05)	236.21(03)	−0.04	$5d^9 6s^2\ ^2$D	5/2	$5d^9 6s6p\ ^4$F°	3/2		New
1	237.58(06)	237.63(02)	−0.05	$5d^9 6s^2\ ^2$D	5/2	$5d^9 6s6p\ ^2$D°	3/2		PS
1	238.81(05)	238.78(02)	0.03	$5d^9 6s^2\ ^2$D	5/2	$5d^9 6s6p\ ^4$D°	7/2		PS
18	242.76(05)	242.8(03)	−0.04	$5d^{10} 6s\ ^2$S	1/2	$5d^{10} 6p\ ^2$P°	3/2	Bl. (Au II, Fe II)	PS
1	252.54(06)	252.49(04)	0.05	$5d^{10} 6p\ ^2$P°	3/2	$5d^9 6s6d$ 15	5/2		New
18	253.49(05)	253.52(02)	−0.03	$5d^{10} 6p\ ^2$P°	1/2	$5d^9 6s6d$ 31	3/2		New
1	256.85(05)	256.88(02)	−0.03	$5d^{10} 6p\ ^2$P°	1/2	$5d^9 6s6d$ 5	3/2		New
19	258.93(05)	258.96(04)	−0.03	$5d^9 6s6p\ ^4$P°	5/2	$5d^9 6s6d$ 15	5/2		PS
21	263.76(05)	263.74(02)	0.02	$5d^{10} 6p\ ^2$P°	3/2	$5d^9 6s7s$ 33	5/2	Bl. (Fe II)	New
30	266.61(05)	266.64(02)	−0.03	$5d^{10} 6p\ ^2$P°	3/2	$5d^9 6s6d$ 12	5/2	Bl. (Fe I)	New
42	267.23(05)	267.24(03)	−0.01	$5d^9 6s^2\ ^2$D	3/2	$5d^9 6s6p\ ^2$P°	3/2		New
57	267.54(05)	267.59(03)	−0.05	$5d^{10} 6s\ ^2$S	1/2	$5d^{10} 6p\ ^2$P°	1/2		PS
74	280.06(06)	280.1(03)	−0.04	$5d^{10} 6p\ ^2$P°	1/2	$5d^{10} 12d\ ^2$D	3/2	Bl. (Fe II, N III)	PS
57	301.76(05)	301.75(04)	0.01	$5d^9 6s6p\ ^4$F°	7/2	$5d^9 6s6d$ 12	5/2		PS
76	302.91(05)	302.91(03)	0.0	$5d^9 6s^2\ ^2$D	5/2	$5d^9 6s6p\ ^4$P°	5/2		PS
58	304.46(05)	304.46(03)	0.0	$5d^9 6s6p\ ^4$F°	5/2	$5d^9 6s6d$ 14	3/2		New
76	306.22(05)	306.23(04)	−0.01	$5d^9 6s6p\ ^4$F°	5/2	$5d^9 6s6d$ 13	3/2	Broad	New
59	308.19(05)	308.18(04)	0.01	$5d^9 6s6p\ ^4$D°	5/2	$5d^9 6s6d$ 13	3/2		New
84	312.29(05)	312.29(03)	0.0	$5d^9 6s^2\ ^2$D	5/2	$5d^{10} 6p\ ^2$P°	3/2		PS
59	312.5(05)	312.53(03)	−0.03	$5d^{10} 6p\ ^2$P°	3/2	$5d^{10} 14s\ ^2$S	1/2	Bl. (N III)	PS
84	313.66(05)	313.61(03)	0.05	$5d^{10} 6p\ ^2$P°	3/2	$5d^{10} 12d\ ^2$D	3/2	Bl. (Fe I, Fe II)	PS
59	314.8(05)	314.78(03)	0.02	$5d^9 6s^2\ ^2$D	3/2	$5d^9 6s6p\ ^4$P°	1/2	Bl. (Fe I)	New
85	323.08(05)	323.08(04)	0.0	$5d^9 6s6p\ ^4$F°	7/2	$5d^9 6s6d$ 25	9/2	Bl. (Fe I)	ED
59	323.7(05)	323.67(03)	0.03	$5d^9 6s6p\ ^4$P°	5/2	$5d^{10} 12d\ ^2$D	3/2	Bl. (Fe II)	New
88	324.75(06)	324.75(06)	0.0	$5d^9 6s6p\ ^4$F°	5/2	$5d^9 6s6d$ 11	5/2		New
59	325.33(06)	325.31(04)	0.02	$5d^9 6s6p\ ^4$F°	5/2	$5d^9 6s6d$ 10	3/2	Bl. (Fe I)	PS
88	326.46(05)	326.5(04)	−0.04	$5d^9 6s6p\ ^4$F°	5/2	$5d^9 6s6d$ 31	3/2		ED
88	331.18(07)	331.18(06)	0.0	$5d^9 6s6p\ ^4$D°	5/2	$5d^9 6s6d$ 6 (26)	5/2	Doubly classified	New
88	331.18(07)	331.18(06)	0.0	$5d^9 6s6p\ ^4$D°	5/2	$5d^9 6s6d$ 27	3/2	Doubly classified	New
59	332.05(05)	332.01(04)	0.04	$5d^{10} 6p\ ^2$P°	1/2	$5d^{10} 7d\ ^2$D	3/2		ED
61	338.21(07)	338.2(06)	0.01	$5d^9 6s6p\ ^4$P°	3/2	$5d^9 6s6d$ 6 (26)	5/2	Bl. (Fe I, O III)	PS
61	338.21(07)	338.2(06)	0.01	$5d^9 6s6p\ ^4$P°	3/2	$5d^9 6s6d$ 27	3/2	Bl. (Fe I, O III)	PS
90	342.2(05)	342.19(04)	0.01	$5d^9 6s6p\ ^4$P°	5/2	$5d^{10} 9d\ ^2$D	5/2		PS
61	353.59(05)	353.58(03)	0.01	$5d^9 6s6p\ ^2$F°	7/2	$5d^9 6s6d$ 16	5/2		PS
90	362.28(05)	362.29(05)	−0.01	$5d^9 6s6p\ ^4$F°	3/2	$5d^9 6s7s$ 33	5/2	New classification	ED
61	368.09(05)	368.09(05)	0.0	$5d^9 6s6p\ ^4$F°	7/2	$5d^{10} 11d\ ^2$D	5/2	Broad	New
62	368.61(07)	368.63(05)	−0.02	$5d^9 6s6p\ ^4$D°	5/2	$5d^{10} 14d\ ^2$D	3/2	Broad	New
62	368.61(07)	368.58(04)	0.03	$5d^9 6s6p\ ^4$D°	5/2	$5d^{10} 14d\ ^2$D	5/2	Broad	New
90	370.05(05)	370.06(04)	−0.01	$5d^9 6s6p\ ^2$D°	5/2	$5d^9 6s6d$ 12	5/2	Bl. (Fe I)	PS
62	371.24(05)	371.25(04)	−0.01	$5d^9 6s6p\ ^4$D°	5/2	$5d^{10} 13d\ ^2$D	3/2	Bl. (O III)	New
92	379.58(05)	379.58(05)	0.0	$5d^{10} 6p\ ^2$P°	3/2	$5d^{10} 7d\ ^2$D	5/2		PS
62	380.15(05)	380.17(04)	−0.02	$5d^{10} 6p\ ^2$P°	3/2	$5d^{10} 7d\ ^2$D	3/2	Broad	PS
92	380.47(05)	380.47(03)	0.0	$5d^9 6s6p\ ^2$F°	7/2	$5d^9 6s7s$ 33	5/2	Obscured	New
62	386.53(05)	386.52(04)	0.01	$5d^9 6s6p\ ^2$F°	7/2	$5d^9 6s6d$ 12	5/2	Bl. (Fe I)	PS
92	389.81(05)	389.82(05)	−0.01	$5d^9 6s6p\ ^4$P°	5/2	$5d^9 6s7s\ ^4$D	7/2	Bl. (Fe I)	PS
62	392.78(06)	392.77(05)	0.01	$5d^9 6s6p\ ^4$D°	7/2	$5d^9 6s6d$ 25	9/2	Bl. (Fe I)	ED
93	398.67(05)	398.67(05)	0.0	$5d^9 6s6p\ ^2$D°	5/2	$5d^9 6s6d$ 8 (29)	7/2	Bl. (Fe II)	PS
93	399.12(08)	399.12(09)	0.0	$5d^9 6s6p\ ^4$F°	5/2	$5d^9 6s7s\ ^2$D	5/2	Broad	PS
93	399.12(08)	399.16(05)	−0.04	$5d^9 6s6p\ ^2$D°	3/2	$5d^9 6s6d$ 5	3/2	Broad	PS
65	404.1(05)	404.11(04)	−0.01	$5d^9 6s^2\ ^2$D	3/2	$5d^9 6s6p\ ^4$F°	5/2	Bl. (Fe I)	PS
94	404.6(05)	404.6(05)	0.0	$5d^9 6s6p\ ^4$P°	3/2	$5d^{10} 11s\ ^2$S	1/2	Bl. (Fe I)	New
69	406.46(05)	406.46(05)	0.0	$5d^{10} 6p\ ^2$P°	1/2	$5d^{10} 6d\ ^2$D	3/2	Bl. (Fe I)	ED
95	408.4(05)	408.4(05)	0.0	$5d^9 6s6p\ ^4$F°	5/2	$5d^9 6s7s\ ^4$D	3/2	Bl. (Fe I)	PS

Table 2
(Continued)

Rel. Intens.	$\lambda_{obs.}$	λ_{Ritz}	$\Delta\lambda$	Lower Level	J_l	Upper Level	J_u	Note	References
69	429.47(06)	429.47(05)	0.0	$5d^9 6s6p\ ^4\mathrm{D}^\circ$	1/2	$5d^9 6s6d$ 14	3/2		PS
95	431.53(05)	431.53(05)	0.0	$5d^9 6s6p\ ^4\mathrm{F}^\circ$	7/2	$5d^9 6s7s\ ^4\mathrm{D}$	5/2		PS
69	433.34(05)	433.36(05)	−0.02	$5d^9 6s6p_{1/2}\ ^2\mathrm{F}^\circ$	5/2	$5d^9 6s6d$ 17	3/2		PS
95	448.96(06)	448.93(05)	0.03	$5d^9 6s6p\ ^2\mathrm{D}^\circ$	3/2	$5d^{10} 14d\ ^2\mathrm{D}$	3/2	Bl. (Fe I)	New
69	452.82(05)	452.82(04)	0.0	$5d^9 6s6p\ ^2\mathrm{D}^\circ$	3/2	$5d^{10} 13d\ ^2\mathrm{D}$	3/2		New
95	455.83(06)	455.84(04)	−0.01	$5d^9 6s6p\ ^2\mathrm{D}^\circ$	3/2	$5d^{10} 14s\ ^2\mathrm{S}$	1/2	Bl. (Cr II)	New
69	472.16(06)	472.17(06)	−0.01	$5d^9 6s6p\ ^4\mathrm{D}^\circ$	1/2	$5d^9 6s6d$ 10	3/2	Bl. (Fe I)	PS
99	479.26(05)	479.25(05)	0.01	$5d^{10} 6p\ ^2\mathrm{P}^\circ$	3/2	$5d^{10} 6d\ ^2\mathrm{D}$	5/2	Obscured	PS
69	482.93(05)	482.94(05)	−0.01	$5d^9 6s6p\ ^2\mathrm{F}^\circ$	7/2	$5d^{10} 14d\ ^2\mathrm{D}$	5/2		New
99	486.62(05)	486.6(05)	0.02	$5d^9 6s6p\ ^4\mathrm{D}^\circ$	1/2	$5d^9 6s6d$ 5	3/2	Broad	New
70	493.63(06)	493.63(05)	0.0	$5d^9 6s6p\ ^2\mathrm{F}^\circ$	7/2	$5d^{10} 12d\ ^2\mathrm{D}$	5/2	Bl. (Cr I)	New
99	495.75(05)	495.75(05)	0.0	$5d^9 6s6p\ ^2\mathrm{P}^\circ$	3/2	$5d^9 6s6d$ 14	3/2	Bl. (Fe I)	PS
70	506.77(05)	506.77(05)	0.0	$5d^9 6s6p\ ^2\mathrm{D}^\circ$	5/2	$5d^{10} 9d\ ^2\mathrm{D}$	5/2	Bl. (Fe II)	New
99	523.01(05)	523.01(05)	0.0	$5d^9 6s6p\ ^4\mathrm{F}^\circ$	9/2	$5d^9 6s7s\ ^4\mathrm{D}$	7/2		PS
70	549.99(05)	549.97(05)	0.02	$5d^9 6s6p_{1/2}\ ^2\mathrm{F}^\circ$	5/2	$5d^9 6s6d$ 31	3/2		New
70	550.56(07)	550.55(07)	0.01	$5d^9 6s6p\ ^4\mathrm{P}^\circ$	1/2	$5d^{10} 9d\ ^2\mathrm{D}$	3/2	Broad	New
70	550.56(07)	550.56(07)	0.0	$5d^9 6s6p_{1/2}\ ^2\mathrm{F}^\circ$	5/2	$5d^9 6s6d$ 30	5/2	Broad	New
100	553.18(05)	553.18(05)	0.0	$5d^9 6s6p\ ^2\mathrm{P}^\circ$	3/2	$5d^9 6s6d$ 16	5/2		PS
70	572.91(05)	572.91(05)	0.0	$5d^9 6s6p\ ^2\mathrm{D}^\circ$	3/2	$5d^{10} 9s\ ^2\mathrm{S}$	1/2		New
100	586.15(06)	586.13(05)	0.02	$5d^9 6s6p\ ^4\mathrm{D}^\circ$	3/2	$5d^{10} 14s\ ^2\mathrm{S}$	1/2		New
71	589.82(05)	589.83(05)	−0.01	$5d^9 6s6p\ ^4\mathrm{D}^\circ$	3/2	$5d^{10} 12d\ ^2\mathrm{D}$	5/2	Bl. (Fe II)	New
100	595.7(05)	595.69(05)	0.01	$5d^9 6s6p\ ^4\mathrm{D}^\circ$	7/2	$5d^9 6s7s\ ^4\mathrm{D}$	7/2		PS
71	621.93(05)	621.93(05)	0.0	$5d^9 6s6p\ ^2\mathrm{P}^\circ$	3/2	$5d^9 6s7s$ 33	5/2	Bl. (Fe I)	New
100	623.03(05)	623.03(05)	0.0	$5d^{10} 7p\ ^2\mathrm{P}^\circ$	3/2	$5d^9 6s6d$ 30	5/2		New
71	627.78(05)	627.77(05)	0.01	$5d^9 6s^2\ ^2\mathrm{D}$	3/2	$5d^{10} 6p\ ^2\mathrm{P}^\circ$	1/2		PS
100	639.96(05)	639.97(05)	−0.01	$5d^9 6s6p\ ^4\mathrm{D}^\circ$	1/2	$5d^{10} 9d\ ^2\mathrm{D}$	3/2	Bl.(Fe I, N II)	New
71	721.01(05)	721.01(05)	0.0	$5d^9 6s6p\ ^4\mathrm{D}^\circ$	3/2	$5d^{10} 8d\ ^2\mathrm{D}$	3/2		New
100	735.35(06)	735.35(06)	0.0	$5d^9 6s6p_{3/2}\ ^2\mathrm{F}^\circ$	5/2	$5d^{10} 13d\ ^2\mathrm{D}$	3/2		New
71	749.34(05)	749.33(05)	0.01	$5d^9 6s6p_{3/2}\ ^2\mathrm{F}^\circ$	5/2	$5d^{10} 12d\ ^2\mathrm{D}$	5/2		New
100	749.53(05)	749.53(05)	0.0	$5d^9 6s6p_{3/2}\ ^2\mathrm{F}^\circ$	5/2	$5d^{10} 12d\ ^2\mathrm{D}$	3/2	Obscured	PS
72	751.08(05)	751.08(05)	0.0	$5d^{10} 6p\ ^2\mathrm{P}^\circ$	3/2	$5d^{10} 7s\ ^2\mathrm{S}$	1/2		PS
100	753.24(05)	753.24(05)	0.0	$5d^9 6s6p\ ^2\mathrm{P}^\circ$	3/2	$5d^9 6s6d$ 5	3/2	Broad	New

Note. Air wavelengths and uncertainties (in parentheses) are reported in nm. The intensities are normalized to a 0–100 scale (see Section 2.2). Level labels are taken from the most recent literature in the NIST database (Kramida et al. 2020), and Ritz wavelengths are calculated from the experimental level energies in Table 3.

Atomic Spectra Database (ASD; Kramida et al. 2020). Three pairs of lines in Fe II and nine pairs of lines in Fe I were found that share the same upper levels and are present in the same current-driven portion of the discharge as used to report gold intensities. Without the efficiency correction applied, the intensity ratios are within a factor of 7 of the known A value ratios. With the correction applied, the ratios are within a factor of 3 of the known A value ratio. As the gold lines reported in Section 3 were observed in the order they are listed, it is also possible that degradation of the gold plating reduced the observed Au counts as the wavelength range increased. Considering these complications, the reported gold intensities are sufficient for a qualitative discussion of the lines but should not be used to calculate A value ratios of high quality.

Lastly, the intensities of the Au I and Au II lines were normalized on the same 0–100 relative scale such that the strongest lines postcorrection are set to 100. When gold wavelengths may be affected by neighboring transitions from other species, the element and charge state of the species contributing to the blended line is indicated, e.g., Bl. (Fe I). Labels "broad" and "obscured" indicate when an observed line is noticeably wider than other similar transitions or when a line is partially obscured by the strength of a nearby transition. Lines with multiple possible classifications are marked as "doubly classified." Additionally, horizontal lines separate the wavelength ranges observed by the spectrometer in Tables 2 and 4. Though all three probes were used in the line identification process, all gold wavelengths and intensities reported in Sections 3.1–3.2 are taken from the spectra of the second gold probe at a position 6 cm inside the edge of the plasma (CTH shot numbers 18113008–18113025).

3. Results

3.1. Au I

In total, 86 Au I lines are attributed to 90 possible transitions (Table 2) involving 62 levels (Table 3). The total uncertainties in the line positions are given in parentheses, and levels of odd

Table 3
Energy Levels of Au I

Level	$E_{exp.}$	$E_{lit.}$	$(E_{exp.} - E_{lit.})$	Number of Lines	Reference
$5d^{10}6s\ ^2S_{1/2}$	0.0	0.0	0.0	3	ED
$5d^{9}6s^2\ ^2D_{5/2}$	9161.0(5.0)	9161.18	−0.18	8	ED
$5d^{9}6s^2\ ^2D_{3/2}$	21,434.6(4.0)	21,435.19	−0.59	4	ED
$5d^{10}6p\ ^2P^\circ_{1/2}$	37,359.5(4.0)	37,358.99	0.51	6	ED
$5d^{10}6p\ ^2P^\circ_{3/2}$	41,173.7(4.0)	41,174.61	−0.91	8	ED
$5d^{9}6s6p\ ^4P^\circ_{5/2}$	42,164.1(5.0)	42,163.53	0.57	5	ED
$5d^{9}6s6p\ ^4F^\circ_{7/2}$	45,537.0(6.0)	45,537.19	−0.19	2	ED
$5d^{9}6s6p\ ^4F^\circ_{5/2}$	46,173.1(4.0)	46,174.98	−1.88	5	ED
$5d^{9}6s6p\ ^4D^\circ_{5/2}$	46,379.5(5.0)	46,379.0	0.5	6	PS
$5d^{9}6s6p\ ^4P^\circ_{3/2}$	47,006.0(7.0)	47,007.43	−1.43	3	ED
$5d^{9}6s6p\ ^4F^\circ_{9/2}$	48,694.7(6.0)	48,697.15	−2.45	1	ED
$5d^{9}6s6p\ ^4D^\circ_{7/2}$	51,027.1(6.0)	51,028.89	−1.79	3	ED
$5d^{9}6s6p\ ^2D^\circ_{3/2}$	51,230.3(5.0)	51,231.53	−1.23	5	ED
$5d^{9}6s6p\ ^4F^\circ_{3/2}$	51,484.0(6.0)	51,485.0	−1.0	2	PS
$5d^{9}6s6p\ ^2D^\circ_{5/2}$	51,651.7(5.0)	51,653.9	−2.2	3	ED
$5d^{9}6s6p\ ^2F^\circ_{7/2}$	52,802.1(4.0)	52,802.1	0.0	6	ED
$5d^{9}6s6p\ ^4P^\circ_{1/2}$	53,193.9(5.0)	53,196.32	−2.42	2	BG
$5d^{10}7s\ ^2S_{1/2}$	54,484.14(4.5)	54,485.24	−1.1	1	ED
$5d^{9}6s6p\ ^4D^\circ_{1/2}$	55,731.1(4.0)	55,732.5	−1.4	4	ED
$5d^{9}6s6p\ ^4D^\circ_{3/2}$	56,105.1(5.0)	56,105.75	−0.65	2	ED
$5d^{9}6s6p_{1/2}\ ^2F^\circ_{5/2}$	58,614.9(2.5)	58,616.76	−1.86	2	ED
$5d^{9}6s6p\ ^2P^\circ_{3/2}$	58,843.1(5.0)	58,845.41	−2.31	3	ED
$5d^{9}6s6p_{3/2}\ ^2F^\circ_{5/2}$	59,712.8(4.0)	59,713.2	−0.4	3	PS
$5d^{10}7p\ ^2P^\circ_{1/2}$		60,032.85		0	BG
$5d^{10}7p\ ^2P^\circ_{3/2}$	60,726.9(4.0)	60,728.49	−1.59	1	BG
$5d^{9}6s6p\ ^2D^\circ_{5/2}$		61,255.1		0	ED
$5d^{9}6s6p\ ^2D^\circ_{3/2}$		61,563.3		0	PS
$5d^{10}6d\ ^2D_{3/2}$	61,955.0(5.0)	61,951.6	3.4	1	ED
$5d^{10}6d\ ^2D_{5/2}$	62,033.6(5.0)	62,033.7	−0.1	1	ED
$5d^{9}6s6p\ ^2P^\circ_{3/2}$	63,003.7(4.0)	63,005.1	−1.4	3	PS
$5d^{10}8s\ ^2S_{1/2}$		64,742.4		0	ED
$5d^{10}8p\ ^2P^\circ_{1/2}$		66,605.3		0	PS
$5d^{10}8p\ ^2P^\circ_{3/2}$		66,910.3		0	PS
$5d^{10}7d\ ^2D_{3/2}$	67,470.0(5.0)	67,469.4	0.6	2	ED
$5d^{10}5f\ ^2F^\circ_{7/2}$		67,485.3		0	PS
$5d^{10}5f\ ^2F^\circ_{5/2}$	67,485.0(11.0)	67,490.0	−5.0	1	PS
$5d^{10}7d\ ^2D_{5/2}$	67,511.0(6.0)	67,510.7	0.3	1	ED
$5d^{9}6s7s\ ^4D_{7/2}$	67,809.6(6.0)	67,811.5	−1.9	2	ED
$5d^{10}9s\ ^2S_{1/2}$	68,680.3(5.0)	68,680.5	−0.2	1	ED
$5d^{9}6s7s\ ^4D_{5/2}$	68,704.0(7.0)	68,705.1	−1.1	1	ED
$5d^{10}8d\ ^2D_{3/2}$	69,970.62(4.6)	69,971.3	−0.68	1	ED
$5d^{10}8d\ ^2D_{5/2}$		70,007.6		0	ED
$5d^{10}10s\ ^2S_{1/2}$		70,617.3		0	ED
$5d^{9}6s7s\ ^4D_{3/2}$	70,652.0(5.0)	70,653.3	−1.3	1	ED
$5d^{9}6s7s\ ^2D_{5/2}$	71,221.0(7.0)	71,222.0	−1.0	1	ED
$5d^{10}9d\ ^2D_{3/2}$	71,352.6(4.0)	71,354.4	−1.8	2	ED
$5d^{10}9d\ ^2D_{5/2}$	71,379.0(6.0)	71,380.4	−1.4	2	ED
$5d^{10}11s\ ^2S_{1/2}$	71,715.0(7.0)	71,713.8	1.2	1	ED
$5d^{10}10d\ ^2D_{3/2}$		72,163.8		0	ED
$5d^{10}10d\ ^2D_{5/2}$		72,170.8		0	ED
$5d^{10}12s\ ^2S_{1/2}$		72,395.9		0	PS
$5d^{10}11d\ ^2D_{3/2}$		72,690.1		0	PS
$5d^{10}11d\ ^2D_{5/2}$	72,696.4(7.4)	72,694.8	1.6	1	PS
$5d^{10}13s\ ^2S_{1/2}$		72,847.5		0	PS
$5d^{10}12d\ ^2D_{3/2}$	73,050.8(4.0)	73,051.0	−0.2	4	ED
$5d^{10}12d\ ^2D_{5/2}$	73,054.4(4.0)	73,054.8	−0.4	3	PS
$5d^{10}14s\ ^2S_{1/2}$	73,161.5(5.0)	73,162.1	−0.6	3	PS

Table 3
(Continued)

Level	$E_{exp.}$	$E_{lit.}$	$(E_{exp.} - E_{lit.})$	Number of Lines	Reference
$5d^{10}13d\ ^2D_{3/2}$	73,308.1(4.0)	73,308.1	0.0	3	ED
$5d^{10}13d\ ^2D_{5/2}$		73,312.6		0	PS
$5d^{10}14d\ ^2D_{3/2}$	73,499.0(5.0)	73,500.4	−1.4	2	PS
$5d^{10}14d\ ^2D_{5/2}$	73,503.0(5.0)	73,502.5	0.5	2	PS
$5d^9 6s6d\ 5_{3/2}$	76,276.0(4.0)	76,278.0	−2.0	4	PS
$5d^9 6s6d\ 25_{9/2}$	76,480.0(6.0)	76,481.95	−1.95	2	ED
$5d^9 6s6d\ 6\ (26)_{5/2}$	76,566.0(7.0)	76,566.22	−0.22	2	ED
$5d^9 6s6d\ 27_{3/2}$	76,566.0(7.0)	76,568.07	−2.07	2	ED
$5d^9 6s6d\ 7\ (28)_{11/2}$		76,569.73		0	ED
$5d^9 6s6d\ 8\ (29)_{7/2}$	76,728.0(6.0)	76,731.99	−3.99	1	ED
$5d^9 6s6d\ 30_{5/2}$	76,773.1(3.0)	76,774.6	−1.5	1	ED
$5d^9 6s6d\ 31_{3/2}$	76,792.6(3.0)	76,793.11	−0.51	3	ED
$5d^9 6s6d9\ (32)_{9/2}$		76,829.8		0	ED
$5d^9 6s6d\ 10_{3/2}$	76,904.0(5.0)	76,906.4	−2.4	2	PS
$5d^9 6s6d\ 11_{5/2}$	76,957.0(7.0)	76,955.0	2.0	1	PS
$5d^9 6s6d\ 12_{5/2}$	78,666.9(5.0)	78,667.8	−0.9	4	PS
$5d^9 6s6d\ 13_{3/2}$	78,819.0(5.0)	78,819.9	−0.9	2	PS
$5d^9 6s6d\ 14_{3/2}$	79,008.9(5.0)	79,010.2	−1.3	3	PS
$5d^9 6s7s\ 33_{5/2}$	79,078.2(4.0)	79,080.3	−2.1	4	ED
$5d^9 6s6d\ 15_{5/2}$	80,768.0(7.0)	80,772.7	−4.7	2	PS
$5d^9 6s6d\ 16_{5/2}$	81,076.0(5.0)	81,076.8	−0.8	2	PS
$5d^9 6s6d\ 17_{3/2}$	81,683.7(0.005)	81,683.7	0.0	1	PS
$5d^9 6s7s\ 34_{3/2}$		86,507.68		0	ED

Note. Level energies are reported in units of cm^{-1}, and literature values are taken from the listed references. Experimental uncertainties, shown in parentheses, are calculated by the LOPT code from the uncertainties of the transitions associated with each level. Where possible, level labels have been updated according to the NIST database (Kramida et al. 2020). All energies and uncertainties are presented with respect to the ground term. Levels fixed in the level optimization are denoted by an uncertainty of 0.005 cm^{-1}. The number of lines defining each level is listed.

parity are denoted by the "°" symbol. Where available, a reference to previous detections of each line with the conventions of Platt & Sawyer (1941, hereafter PS), Ehrhardt & Davis (1971, hereafter ED), Brown & Ginter (1978, hereafter BG), and Rosberg & Wyart (1997, hereafter RW) are provided. In both PS and ED, the L and S information of the $5d^9 6s6d$ levels is unavailable, and the authors adopted independent numeric labeling schemes. Where applicable, labels from both PS and ED are listed, with the lower of the two numbers corresponding to the label from Platt & Sawyer (1941). Forty-three Au I lines were unobserved by the references compiled here and are labeled "new." For both Au I and Au II, lines with $\lambda > 550$ nm are considered tentative, as nickel measurements at a 6 cm probe tip depth were not collected in this range.

As a check on the identifications in Table 2, level energies are recalculated using the level assignments available in the literature and the measured wavelengths. We used the level optimization code LOPT (Kramida 2011), which optimizes the level energies given a set of observed wavelengths. The uncertainty in the level energies is derived from the experimental uncertainties in the associated transitions. The recalculated level energies are collected in Table 3 and compared to the available literature. All calculated energies are reported with respect to the ground state of the system, $5d^{10}6s\ (^2S_{1/2})$, which is fixed at both zero energy and zero uncertainty. Using the ground state as the only constraint, the uncertainties in the level energies are, on average, ± 6.4 cm^{-1} from LOPT, and the average difference between the experimental and literature energies is 4.2 cm^{-1}. By fixing the level $5d^9 6s6d\ 34_{3/2}$ (86,507.68 ± 0.005 cm^{-1}), the average uncertainty and energy difference are reduced to 5.2 and 1.4 cm^{-1}, respectively. Using both the literature and the calculated level energies, the average difference between the observed and Ritz wavelengths is 0.02 nm.

In Au I, the observed transitions involve the following single-electron valence configurations: ns ($n = 6, 7, 9, 11, 14$), np ($n = 6, 7$), and 1–2 J levels from each of the nd ($n = 6$–9, 11–14) configurations. No transitions involving the ns ($n = 8$, 10, 12, 13) levels from PS and ED were observed. This is unexpected, as transitions from these levels were weak in both PS and ED but are absent entirely from the present work. For transitions involving the nd ($n = 6$–9) configurations, the splitting between $J = \frac{3}{2}$ and $\frac{5}{2}$ is large enough that transitions from individual nd (^2D_J) levels are resolvable. For $n = 11$–14, the splitting between the two levels is smaller than the resolution of the spectrometer; however, the line profiles do not indicate contributions from decays of both the $J = \frac{3}{2}$ and $\frac{5}{2}$ levels.

For the open $5d$ shell, transitions were observed to originate from one of the $5d^9 6s7s$ levels, 16 $5d^9 6s6d$ levels, and 18 $5d^9 6s6p$ levels of Platt & Sawyer (1941) and Ehrhardt & Davis (1971). It is interesting that the transitions involve many of the $5d^9 6s6p$ levels that were *not* seen by Ehrhardt & Davis (1971): $^4D^\circ_{5/2}$, $^4F^\circ_{3/2}$, $^4D^\circ_{1/2}$, $^4D^\circ_{3/2}$, $^2F^\circ_{5/2}$, and $^2P^\circ_{3/2}$. For the $5d^9 6s6d$ configuration, 16 of the 18 known levels each involve

Table 4
Observed Transitions in Au II

Rel. Intens.	$\lambda_{obs.}$	λ_{Ritz}	$\Delta\lambda$	Lower Level	J_l	Upper Level	J_u	Note	References
1	197.8(05)	197.77(03)	0.03	$5d^8 6s^2\ ^3F$	3	$5d^8(^3P)6s6p\ ^5P°$	3		New
0	200.11(05)	200.1(04)	0.01	$5d^9 6s\ ^3D$	3	$5d^9 6p\ (5/2,1/2)°$	3	Bl. (Fe II)	RW
1	204.06(05)	204.04(03)	0.02	$5d^8 6s^2\ ^3P$	0	$5d^8 6s6p\ 5°$	1		RW
0	204.29(05)	204.29(05)	0.0	$5d^8 6s^2\ ^1G$	4	$5d^8(^3F)6s6p\ ^1G°$	4	Bl. (O II)	New
1	204.48(05)	204.46(01)	0.02	$5d^9 6s\ ^3D$	1	$5d^9 6p\ (3/2,1/2)°$	2	Broad	RW
1	208.27(05)	208.21(0)	0.06	$5d^9 6s\ ^3D$	3	$5d^9 6p\ (5/2,1/2)°$	2	Bl. (Au III)	RW
1	219.04(05)	219.05(0)	−0.01	$5d^9 6s\ ^3D$	1	$5d^9 6p\ (5/2,3/2)°$	1		PS
1	228.3(07)	228.32(04)	−0.02	$5d^8 6s^2\ ^3P$	2	$5d^8 6s6p\ 2°$	3		RW
1	228.3(07)	228.3(07)	0.0	$5d^9 6s\ ^1D$	2	$5d^9 6p\ (5/2,3/2)°$	1		RW
1	229.11(08)	229.09(03)	0.02	$5d^8(^3F)6s6p\ ^5D°$	3	$5d^9 6d\ (3/2,5/2)$	2	Bl. (O II, C III)	PS
1	229.11(08)	229.1(05)	0.01	$5d^9 6p\ (5/2,1/2)°$	3	$5d^9 7s\ (5/2,1/2)$	2	Bl. (O II, C III)	PS
1	230.45(07)	230.48(04)	−0.03	$5d^9 6p\ (5/2,3/2)°$	3	$5d^9 6d\ (5/2,5/2)$	4		RW
1	230.45(07)	230.48(04)	−0.03	$5d^8(^3F)6s6p\ ^5D°$	3	$5d^9 6d\ (3/2,5/2)$	4		RW
2	230.75(05)	230.75(05)	0.0	$5d^8 6s^2\ ^1D$	2	$5d^8(^3P)6s6p\ ^5S°$	2	Bl. (Fe II)	New
2	234.05(07)	234.0(03)	0.05	$5d^9 6p\ (5/2,3/2)°$	3	$5d^9 6d\ (5/2,3/2)$	3	Broad	RW
2	234.05(07)	234.02(03)	0.03	$5d^9 6p\ (3/2,3/2)°$	2	$5d^9 6d\ (3/2,3/2)$	1	Broad	RW
2	236.45(05)	236.48(03)	−0.03	$5d^9 6p\ (5/2,3/2)°$	3	$5d^9 6d\ (5/2,3/2)$	2		RW
2	237.35(05)	237.35(05)	0.0	$5d^8 6s^2\ ^3F$	2	$5d^8(^3P)6s6p\ ^5P°$	1		New
18	242.76(05)	242.76(05)	0.0	$5d^8 6s6p\ 2°$	3	$5d^9\ 8s\ (5/2,1/2)$	3	Bl. (Au I, Fe II)	New
2	245.84(05)	245.84(05)	0.0	$5d^8 6s^2\ ^3P$	1	$5d^8 6s6p\ 5°$	2		New
19	249.29(05)	249.25(03)	0.04	$5d^8 6s^2\ ^3F$	2	$5d^8(^3P)6s6p\ ^5D°$	1	Bl. (Fe II)	RW
2	253.35(05)	253.36(04)	−0.01	$5d^9 6p\ (3/2,1/2)°$	1	$5d^9 7s\ (3/2,1/2)$	2	Broad	RW
19	253.8(05)	253.78(02)	0.02	$5d^9 6p\ (3/2,1/2)°$	2	$5d^9 6d\ (5/2,3/2)$	1	Broad	PS
2	255.14(05)	255.14(04)	0.0	$5d^8(^3P)6s6p\ ^5P°$	2	$5d^9 6d\ (3/2,3/2)$	3		PS
19	256.85(05)	256.87(04)	−0.02	$5d^8(^3P)6s6p\ ^5P°$	2	$5d^9 6d\ (3/2,3/2)$	1		New
4	258.93(05)	258.94(03)	−0.01	$5d^9 6p\ (3/2,1/2)°$	1	$5d^9 6d\ (5/2,5/2)$	0		RW
44	260.95(05)	260.97(04)	−0.02	$5d^8 6s^2\ ^3P$	2	$5d^8(^3F)6s6p^5D°$	3	Bl. (Fe I)	New
19	261.76(05)	261.76(04)	0.0	$5d^8 6s^2\ ^3F$	3	$5d^8(^3P)6s6p\ ^5P°$	2	Bl. (Fe II)	New
59	262.5(05)	262.5(05)	0.0	$5d^8 6s^2\ ^1G$	4	$5d^8 6s6p\ 4°$	4	Bl. (Fe II)	New
22	262.76(05)	262.73(04)	0.03	$5d^8 6s^2\ ^3P$	2	$5d^9 6p\ (3/2,3/2)°$	2	Bl. (Fe II)	RW
62	272.15(06)	272.15(05)	0.0	$5d^8(^1D)6s6p\ ^3F°$	2	$5d^9 6d\ (3/2,3/2)$	2		New
31	277.51(05)	277.52(05)	−0.01	$5d^8(^1D)6s6p\ ^3F°$	2	$5d^9 6d\ (3/2,3/2)$	3		New
62	278.11(06)	278.11(06)	0.0	$5d^8 6s^2\ ^3F$	3	$5d^8(^3F)6s6p\ ^5G°$	4	Bl. (Fe I, N II)	RW
38	280.9(06)	280.9(06)	0.0	$5d^8(^3F)6s6p\ ^5D°$	2	$5d^9 6d\ (3/2,5/2)$	3	Broad	New
65	282.41(06)	282.4(04)	0.01	$5d^9 6p\ (3/2,1/2)°$	1	$5d^9 6d\ (5/2,3/2)$	2		New
38	291.39(05)	291.39(05)	0.0	$5d^8 6s^2\ ^3F$	4	$5d^9 6p\ (5/2,3/2)°$	3	Broad	RW
69	292.96(05)	292.96(05)	0.0	$5d^8(^3F)6s6p\ ^5D°$	2	$5d^9 6d\ (3/2,3/2)$	1	Bl. (Fe I)	New
38	306.6(05)	306.6(05)	0.0	$5d^8 6s6p\ 5°$	3	$5d^9\ 8s\ (5/2,1/2)$	3		New
69	307.04(05)	307.04(05)	0.0	$5d^8 6s6p\ 4°$	3	$5d^9 6d\ (3/2,5/2)$	2		New
38	307.96(05)	307.95(04)	0.01	$5d^9 6p\ (3/2,3/2)°$	3	$5d^9 6d\ (5/2,5/2)$	4		New
69	308.96(06)	308.96(05)	0.0	$5d^8 6s6p\ 4°$	3	$5d^9 6d\ (3/2,3/2)$	2	Broad	New
38	310.84(05)	310.81(04)	0.03	$5d^8(^3P)6s6p\ ^5D°$	1	$5d^9 6d\ (3/2,5/2)$	2		New
78	312.29(05)	312.29(05)	0.0	$5d^8 6s^2\ ^3F$	4	$5d^9 6p\ (5/2,3/2)°$	4		RW
38	317.3(05)	317.3(05)	0.0	$5d^9 6p\ (3/2,1/2)°$	2	$5d^9 7s\ (5/2,1/2)$	3		RW
79	323.08(05)	323.08(04)	0.0	$5d^9 6p(3/2,3/2)°$	2	$5d^9 6d\ (5/2,3/2)$	3		PS
38	325.11(05)	325.1(05)	0.01	$5d^8(^3P)6s6p\ ^5P°$	2	$5d^9 7s\ (3/2,1/2)$	2		RW
79	325.33(05)	325.33(04)	0.0	$5d^9 6p\ (3/2,3/2)°$	2	$5d^9 6d\ (5/2,5/2)$	1		New
38	327.84(06)	327.83(04)	0.01	$5d^9 6p\ (3/2,3/2)°$	2	$5d^9 6d\ (5/2,3/2)$	2	Obscured	New
79	330.6(05)	330.6(05)	0.0	$5d^8(^3F)6s6p\ ^5D°$	3	$5d^9 6d\ (5/2,3/2)$	2	Bl. (Fe I)	New
38	338.72(05)	338.71(05)	0.01	$5d^8 6s^2\ ^1D$	2	$5d^8(^3P)6s6p\ ^5P°$	1		New
79	356.47(05)	356.48(04)	−0.01	$5d^8 6s6p\ 5°$	2	$5d^9 6d\ (3/2,5/2)$	2	Bl. (Fe I)	New
38	362.09(05)	362.09(05)	0.0	$5d^8(^3P)6s6p\ ^5P°$	2	$5d^9 6d\ (5/2,5/2)$	3		New
79	363.06(05)	363.04(05)	0.02	$5d^8(^3P)6s6p\ ^5P°$	3	$5d^9 6d\ (3/2,3/2)$	2	Bl. (Fe I)	New
39	363.4(05)	363.39(05)	0.01	$5d^8 6s^2\ ^3F$	2	$5d^9 6p\ (3/2,3/2)°$	3	Bl. (Fe I)	PS
79	363.6(05)	363.58(04)	0.02	$5d^8 6s6p\ 5°$	2	$5d^9 6d\ (3/2,5/2)$	1		New
39	363.88(05)	363.86(05)	0.02	$5d^8(^3P)6s6p\ ^5P°$	3	$5d^9 6d\ (3/2,5/2)$	4		New
79	374.37(06)	374.38(06)	−0.01	$5d^8(^3P)6s6p\ ^5D°$	4	$5d^9 6d\ (3/2,3/2)$	3		New
80	386.53(07)	386.55(06)	−0.02	$5d^8 6s6p\ 2°$	3	$5d^9 6d\ (5/2,5/2)$	4	Bl. (Fe I)	New
80	386.53(07)	386.49(05)	0.04	$5d^8(^3F)6s6p\ ^5G°$	2	$5d^9 6d\ (3/2,5/2)$	2	Bl. (Fe I)	New

Table 4
(Continued)

Rel. Intens.	$\lambda_{obs.}$	λ_{Ritz}	$\Delta\lambda$	Lower Level	J_l	Upper Level	J_u	Note	References
39	394.83(05)	394.85(05)	−0.02	$5d^8(^3F)6s6p\ ^5G°$	2	$5d^96d\ (3/2,5/2)$	1		New
80	404.89(05)	404.89(05)	0.0	$5d^8(^3F)6s6p\ ^5G°$	2	$5d^96d\ (3/2,3/2)$	1		New
40	406.15(05)	406.15(05)	0.0	$5d^8(^3F)6s6p\ ^5F°$	1	$5d^96d\ (3/2,5/2)$	2	Obscured	New
81	408.36(05)	408.37(05)	−0.01	$5d^86s^2\ ^3F$	3	$5d^96p(3/2,1/2)°$	2		ED
40	411.15(05)	411.15(05)	0.0	$5d^86s^2\ ^1G$	4	$5d^96p\ (3/2,3/2)°$	3		PS
81	432.58(05)	432.59(05)	−0.01	$5d^86s^2\ ^3P$	0	$5d^96p\ (3/2,1/2)°$	1	Bl. (Fe I, O II)	New
40	435.96(05)	435.96(05)	0.0	$5d^96p\ (3/2,3/2)°$	3	$5d^97s\ (5/2,1/2)$	2		New
81	446.96(05)	446.95(05)	0.01	$5d^86s6p\ 5°$	1	$5d^96d\ (3/2,5/2)$	1	Bl. (Fe I)	New
40	484.43(05)	484.42(05)	0.01	$5d^86s6p\ 9°$	3	$5d^96d\ (3/2,5/2)$	4		New
81	492.06(05)	492.06(05)	0.0	$5d^86s^2\ ^3F$	3	$5d^96p\ (5/2,3/2)°$	4	Bl. (Fe I)	New
41	501.29(05)	501.3(05)	−0.01	$5d^96d\ (5/2,3/2)$	1	$5d^97p\ (3/2,3/2)°$	2	Broad	New
81	506.71(05)	506.71(05)	0.0	$5d^8(^3P)6s6p\ ^5D°$	1	$5d^96d\ (5/2,5/2)$	2		New
41	540.93(05)	540.93(05)	0.0	$5d^96d\ (5/2,3/2)$	3	$5d^97p\ (3/2,3/2)°$	2		New
81	541.34(05)	541.34(05)	0.0	$5d^86s^2\ ^3F$	2	$5d^96p\ (3/2,1/2)°$	2		PS
41	578.09(05)	578.09(05)	0.0	$5d^96d\ (5/2,3/2)$	1	$5d^97p\ (3/2,1/2)°$	1		New
82	612.19(05)	612.19(05)	0.0	$5d^86s6p\ 2°$	3	$5d^97s\ (5/2,1/2)$	2		New
41	623.03(05)	623.02(05)	0.01	$5d^96d\ (5/2,5/2)$	1	$5d^97p\ (3/2,1/2)°$	1		New
82	660.47(05)	660.47(05)	0.0	$5d^86s6p\ 12°$	3	$5d^96d\ (3/2,5/2)$	2		New
41	703.21(05)	703.21(05)	0.0	$5d^97p\ (5/2,1/2)°$	2	$5d^9\ 8s\ (5/2,1/2)$	2		New
82	717.23(05)	717.22(05)	0.01	$5d^86s6p\ 12°$	2	$5d^96d\ (3/2,3/2)$	1		New
41	733.4(05)	733.4(05)	0.0	$5d^86s6p\ 5°$	2	$5d^96d\ (5/2,3/2)$	1		New
83	764.66(05)	764.66(05)	0.0	$5d^96d\ (5/2,5/2)$	0	$5d^97p\ (3/2,1/2)°$	1	Bl. (Fe II)	New

Note. Air wavelengths and uncertainties (in parentheses) are reported in nm. The intensities are normalized to a 0–100 scale (see Section 2.2). Level labels are taken from Rosberg & Wyart (1997) and, where possible, updated by designations in the NIST database (Kramida et al. 2020). Ritz wavelengths are calculated from the experimental level energies in Table 5.

one to four transitions. No lines involving the levels $5d^96s6d\ 7\ (28)_{11/2}$ or $5d^96s6d\ 9\ (32)_{9/2}$ were observed.

The original studies of these systems used hollow cathodes or spark discharges, and the intensities of lines originating from the $5d^96s6d$ levels in the literature were typically small. In the present work, the intensities of lines from these levels are often comparable to one-electron transitions between low-lying levels during the current-driven portion of the discharge. From the 33 transitions involving the $5d^96s6d$ configuration, 15 were unobserved by both PS and ED. Ten of these newly observed transitions, originating from the $J = \frac{3}{2}, \frac{5}{2}$ levels of the $5d^96s6d$ configuration, decay to the $5d^96s6p$ configuration. The remaining five (new) transitions from $5d^96s6d$ decay to the $5d^96p^2$ and $5d^{10}7p$ configurations and follow a similar trend in their intensities.

In total, the newly identified lines are spread across a wide array of upper levels. Four originate from levels of the $5d^96s7s$ configuration, four occur between low-lying $5d^96s6p$ and $5d^96s^2$ levels, 15 involve the (primarily) $J = \frac{3}{2}, \frac{5}{2}$ levels of $5d^96s6d$ (see above), and 20 transitions are decays from various $5d^{10}ns$ and $5d^{10}nd$ levels. Of these last 20 lines, one decays to the $5d^{10}6p\ (^2P_{1/2})$ level, and the remaining 19 decay to various levels in the $5d^96s6p$ configuration. These transitions, $5d^9(...) \rightarrow 5d^{10}(...)$, expected to be weak by Ehrhardt & Davis (1971) and mostly absent from their data, were not uncommon in the tables of Platt & Sawyer (1941). However, this difference may be explained, as even though both PS and ED utilized hollow cathodes, comparison of their line lists suggests vastly different plasma conditions in the two experiments.

3.2. Au II

In Au II, 76 unique lines arising from 81 possible transitions are reported, 51 of which are unreported in the literature, involving a total of 69 levels. The lines and levels are collected in Tables 4 and 5 and follow the same conventions as previously discussed for Au I. The level energies are taken from the work of Rosberg & Wyart (1997). For some of the Au II levels, L and S information is unavailable due to the low purity of the levels, and the numerical labels are adopted from Rosberg & Wyart (1997). Where possible, the level labels have been updated according to the designations in the NIST database (Kramida et al. 2020).

Au II contains considerably more levels than Au I, and nearly 40% of the known levels are missing representation in the present work. Additionally, as shown in Table 5, many of the levels are defined by only a single transition. The transitions linking the excited states to ground are in the UV shortward of 187 nm, so the level optimization proceeds as follows. We define the ground state ($E = 0 \pm 0\ cm^{-1}$) and connect the observed transitions to ground using the minimum number of levels: $5d^96s\ (^3D_3)$ (15,039.572 cm^{-1}), $5d^86s^2\ (^1G_4)$ (65,307.005 cm^{-1}), $5d^86s6p\ (^3D_1)$ (93,830.264 cm^{-1}), and $5d^97p\ (5/2,\ 1/2)_2$ (119,446.496 cm^{-1}) with the uncertainty quoted by Rosberg & Wyart (0.005 cm^{-1}). Using only these

Table 5
Energy Levels of Au II

Level	$E_{exp.}$	$E_{lit.}$	($E_{exp.} - E_{lit.}$)	Number of Lines	Reference
$5d^{10}\ ^1S_0$	0.0	0.0	0.0	0	RW
$5d^9 6s\ ^3D_3$	15,039.57(0.005)	15,039.57	0.0	3	RW
$5d^9 6s\ ^3D_2$		17,640.62		0	RW
$5d^9 6s\ ^3D_1$	27,765.76(0.004)	27,765.76	0.0	3	RW
$5d^9 6s\ ^1D_2$	29,615.0(14.0)	29,621.25	−6.25	1	RW
$5d^8 6s^2\ ^3F_4$	40,483.0(6.0)	40,478.75	4.25	2	RW
$5d^8 6s^2\ ^3P_2$	48,519.0(6.0)	48,510.89	8.11	3	RW
$5d^8 6s^2\ ^3F_3$	52,178.5(3.0)	52,176.51	1.99	4	RW
$5d^8 6s^2\ ^3F_2$	58,191.63(0.005)	58,191.63	0.0	3	RW
$5d^8 6s^2\ ^3P_0$	58,554.0(6.0)	58,550.23	3.77	2	RW
$5d^8 6s^2\ ^1G_4$	61,387.0(5.0)	61,384.0	3.0	1	RW
$5d^8 6s^2\ ^3P_1$	61,756.0(9.0)	61,749.42	6.58	1	RW
$5d^9 6p\ (5/2,1/2)^\circ_2$	63,053.32(0.005)	63,053.32	0.0	2	RW
$5d^9 6p\ (5/2,1/2)^\circ_3$	64,998.0(10.0)	65,003.59	−5.59	2	RW
$5d^8 6s^2\ ^1G_4$	65,307.0(0.005)	65,307.0	0.0	0	RW
$5d^8 6s^2\ ^1D_2$	70,795.0(11.0)	70,797.19	−2.19	1	RW
$5d^9 6p\ (5/2,3/2)^\circ_4$	72,495.6(4.0)	72,495.13	0.47	2	RW
$5d^9 6p\ (5/2,3/2)^\circ_2$	73,178.29(0.005)	73,178.29	0.0	0	RW
$5d^9 6p\ (5/2,3/2)^\circ_1$	73,403.84(0.005)	73,403.84	0.0	2	RW
$5d^9 6p\ (5/2,3/2)^\circ_3$	74,791.0(6.0)	74,791.48	−0.48	4	RW
$5d^9 6p\ (3/2,1/2)^\circ_2$	76,659.2(1.7)	76,659.7	−0.5	4	RW
$5d^9 6p\ (3/2,1/2)^\circ_1$	81,664.1(5.0)	81,659.83	4.27	4	RW
$5d^9 6p\ (3/2,3/2)^\circ_0$		82,613.78		0	RW
$5d^9 6p\ (3/2,3/2)^\circ_3$	85,702.2(4.0)	85,700.2	2.0	3	RW
$5d^9 6p\ (3/2,3/2)^\circ_1$		85,707.57		0	RW
$5d^9 6p\ (3/2,3/2)^\circ_2$	86,570.0(4.0)	86,565.67	4.33	5	RW
$5d^8(^3F)6s6p\ ^5D^\circ_3$	86,826.0(6.0)	86,821.34	4.66	4	RW
$5d^8(^3F)6s6p\ ^5G^\circ_4$	88,125.0(8.0)	88,126.5	−1.5	1	RW
$5d^8(^3P)6s6p\ ^5P^\circ_2$	90,370.2(5.0)	90,371.0	−0.8	4	RW
$5d^8 6s6p\ 2^\circ_3$	92,303.4(4.0)	92,301.33	2.07	3	RW
$5d^8(^1D)6s6p\ ^3F^\circ_2$	93,529.0(8.0)	93,531.21	−2.21	2	RW
$5d^8(^1D)6s6p\ ^3D^\circ_1$	93,830.26(0.005)	93,830.26	0.0	0	RW
$5d^8(^3F)6s6p\ ^5D^\circ_2$	95,164.0(8.0)	95,160.92	3.08	1	RW
$5d^8(^3F)6s6p\ ^5F^\circ_4$		96,346.88		0	RW
$5d^8(^3F)6s6p\ ^5G^\circ_3$		97,155.64		0	RW
$5d^8 6s6p\ 4^\circ_3$	97,905.0(5.0)	97,904.9	0.1	2	RW
$5d^8(^3P)6s6p\ ^5D^\circ_1$	98,300.0(5.0)	98,298.7	1.3	2	RW
$5d^8 6s6p\ 4^\circ_4$	99,471.0(9.0)	99,474.27	−3.27	1	RW
$5d^8(^3P)6s6p\ ^5P^\circ_1$	100,310.1(9.6)	100,316.97	−6.87	1	RW
$5d^8 6s6p\ 5^\circ_3$	100,878.0(11.0)	100,883.84	−5.84	1	RW
$5d^8(^3F)6s6p\ ^5F^\circ_2$		101,637.14		0	RW
$5d^8 6s6p5^\circ_2$	102,420.2(3.0)	102,418.67	1.53	3	RW
$5d^8(^3P)6s6p\ ^5P^\circ_3$	102,725.0(6.0)	102,726.7	−1.7	3	RW
$5d^8(^3P)6s6p\ ^5D^\circ_4$	102,849.0(9.0)	102,857.48	−8.48	1	RW
$5d^8(^3F)6s6p\ ^5G^\circ_2$	104,597.7(4.0)	104,596.85	0.85	3	RW
$5d^8(^3F)6s6p\ ^5F^\circ_1$	105,850.0(3.0)	105,846.56	3.44	1	RW
$5d^8 6s6p\ 6^\circ_4$		106,569.47		0	RW
$5d^8(^3P)6s6p\ ^5D^\circ_3$		106,713.41		0	RW
$5d^8(^3F)6s6p\ ^5F^\circ_3$		107,238.04		0	RW
$5d^8(^3F)6s6p\ ^1D^\circ_2$		107,239.34		0	RW
$5d^8 6s6p\ 5^\circ_1$	107,549.0(4.0)	107,551.05	−2.05	2	RW
$5d^9 7s\ (5/2,1/2)_3$	108,166.0(5.0)	108,172.95	−6.95	1	RW
$5d^9 7s\ (5/2,1/2)_2$	108,633.6(4.0)	108,631.44	2.16	3	RW
$5d^8 6s6p\ 9^\circ_3$	109,562.7(7.0)	109,560.95	1.75	1	RW
$5d^8(^3P)6s6p\ ^5D^\circ_2$		109,565.33		0	RW
$5d^8 6s6p\ 9^\circ_2$		110,273.09		0	RW
$5d^8 6s6p8^\circ_4$		110,645.77		0	RW
$5d^8(^3P)6s6p\ ^1P^\circ_1$		111,170.45		0	RW
$5d^8(^1G)6s6p\ ^3F^\circ_4$		112,010.36		0	RW
$5d^8 6s6p\ 7^\circ_1$		112,164.17		0	RW
$5d^8(^1D)6s6p\ ^3D^\circ_3$		112,424.94		0	RW
$5d^8(^3P)6s6p\ ^5S^\circ_2$	114,119.0(15.0)	114,121.13	−2.13	1	RW
$5d^8(^1G)6s6p\ ^3F^\circ_3$		114,147.21		0	RW
$5d^8(^3F)6s6p\ ^1G^\circ_4$	114,241.0(12.0)	114,245.88	−4.88	1	RW

Table 5
(Continued)

Level	$E_{exp.}$	$E_{lit.}$	$(E_{exp.} - E_{lit.})$	Number of Lines	Reference
$5d^8 6s6p\ 8°_1$		114,256.2		0	RW
$5d^8 6s6p\ 11°_2$		114,286.01		0	RW
$5d^8 6s6p\ 12°_3$	115,327.9(1.2)	115,327.55	0.35	1	RW
$5d^8 6s6p\ 12°_2$	115,349.8(5.0)	115,348.49	1.31	1	RW
$5d^9 6d\ (5/2,3/2)_1$	116,051.6(3.0)	116,050.55	1.05	4	RW
$5d^8 6s6p\ 13°_2$		116,722.52		0	RW
$5d^9 6d\ (5/2,3/2)_4$		116,946.33		0	RW
$5d^9 6d\ (5/2,3/2)_2$	117,065.0(5.0)	117,065.63	−0.63	4	RW
$5d^9 6d\ (5/2,5/2)_1$	117,298.9(4.0)	117,297.68	1.22	2	RW
$5d^9 6d(5/2,5/2)_5$		117,346.06		0	RW
$5d^9 6d\ (5/2,3/2)_3$	117,512.7(4.0)	117,512.0	0.7	3	RW
$5d^8 6s6p\ 13°_3$		117,661.73		0	RW
$5d^8 6s6p\ 9°_1$		117,686.44		0	RW
$5d^9 6d\ (5/2,5/2)_3$	117,980.0(7.0)	117,983.17	−3.17	1	RW
$5d^9 6d\ (5/2,5/2)_2$	118,029.8(5.0)	118,029.27	0.53	1	RW
$5d^9 6d\ (5/2,5/2)_4$	118,166.0(5.0)	118,168.02	−2.02	3	RW
$5d^8 6s6p\ 14°_3$		118,817.85		0	RW
$5d^8 6s6p\ 10°_1$		119,365.19		0	RW
$5d^9 7p\ (5/2,1/2)°_2$	119,446.5(0.004)	119,446.5	0.0	0	RW
$5d^8(^3P)6s6p\ ^1D°_2$		119,891.66		0	RW
$5d^9 7p\ (5/2,1/2)°_3$		120,257.12		0	RW
$5d^9 6d\ (5/2,5/2)_0$	120,271.1(3.0)	120,269.51	1.59	2	RW
$5d^9 7s\ (3/2,1/2)_1$		120,822.93		0	RW
$5d^8(^1G)6s6p\ ^3F°_2$		120,951.33		0	RW
$5d^9 7s\ (3/2,1/2)_2$	121,121.0(6.0)	121,118.78	2.22	2	RW
$5d^8 6s6p\ 11°_1$		121,862.08		0	RW
$5d^8 6s6p\ 16°_2$		121,870.4		0	RW
$5d^9 7p(5/2,3/2)°_4$		122,656.19		0	RW
$5d^8 6s6p\ 17°_2$		122,814.46		0	RW
$5d^8(^1G)6s6p\ ^3G°_4$		123,062.9		0	RW
$5d^9 7p\ (5/2,3/2)°_3$		123,344.76		0	RW
$5d^9 7p\ (5/2,3/2)°_2$		123,605.66		0	RW
$5d^9 7p\ (5/2,3/2)°_2$		123,605.66		0	RW
$5d^8 6s6p\ 16°_3$		124,012.18		0	RW
$5d^8(^1D)6s6p\ ^3D°_2$		125,103.78		0	RW
$5d^8 6s6p\ 12°_1$		125,156.47		0	RW
$5d^8 6s6p\ 17°_3$		125,241.2		0	RW
$5d^7(^4F)6s\ ^26p\ ^5D°_4$		126,661.8		0	RW
$5d^8 6s6p\ 13°_1$		127,567.36		0	RW
$5d^8 6s6p\ 19°_2$		128,001.87		0	RW
$5d^8 6s6p\ 14°_1$		128,146.04		0	RW
$5d^8 6s6p\ 18°_3$		128,317.31		0	RW
$5d^9 6d\ (3/2,3/2)_1$	129,288.6(4.0)	129,287.88	0.72	3	RW
$5d^9 6d\ (3/2,3/2)_3$	129,552.3(8.0)	129,560.54	−8.24	2	RW
$5d^9 6d(3/2,5/2)_1$	129,916.4(4.0)	129,918.2	−1.8	3	RW
$5d^9 6d\ (3/2,5/2)_4$	130,200.0(7.0)	130,198.66	1.34	2	RW
$5d^9 6d\ (3/2,3/2)_2$	130,262.0(6.0)	130,266.09	−4.09	3	RW
$5d^8 6s6p\ 20°_2$		130,388.83		0	RW
$5d^9 6d\ (3/2,5/2)_2$	130,464.45(0.005)	130,464.45	0.0	5	RW
$5d^9 6d\ (3/2,5/2)_3$	130,753.0(11.0)	130,749.25	3.75	1	RW
$5d^9 6d\ (3/2,3/2)_0$		131,563.73		0	RW
$5d^8(^1G)6s6p\ ^1F°_3$		132,009.57		0	RW
$5d^8 6s6p\ 15°_1$	132,510.92(0.005)	132,510.92	0.0	0	RW
$5d^9 7p\ (3/2,1/2)°_2$		132,923.53		0	RW
$5d^9 7p\ (3/2,1/2)°_1$	133,345.2(3.0)	133,344.72	0.48	3	RW
$5d^9\ 8s\ (5/2,1/2)_3$	133,484.0(10.0)	133,490.3	−6.3	1	RW
$5d^9\ 8s\ (5/2,1/2)_2$	133,663.0(1.0)	133,663.79	−0.79	1	RW
$5d^9 7p\ (3/2,3/2)°_2$	135,994.3(4.0)	135,993.77	0.53	2	RW

Note. Level energies and experimental uncertainties are reported with respect to the ground term in units of cm^{-1}, and literature energies and labels are taken from Rosberg & Wyart (1997). Experimental uncertainties, shown in parentheses, are calculated by the LOPT code from the uncertainties of the transitions associated with each level. Where possible, the level labels have been updated according to the NIST database (Kramida et al. 2020). Levels fixed in the level optimization are denoted by an uncertainty of 0.005 cm^{-1}. The number of lines defining each level is listed.

four levels as constraints, the recalculated level energies have an average uncertainty of 20.3 cm^{-1}, and the average difference between the calculated and literature energies is 7.3 cm^{-1}. As many of the levels are poorly constrained, some of the differences between the optimized and literature energies are larger than the corresponding uncertainties. Additional constraints were provided by fixing nine additional levels (denoted by an uncertainty of 0.005 cm^{-1} in Table 5) with respect to the ground state.

Using these constraints, the recalculated (average) level energy uncertainty of the free levels is reduced from 20.3 to 6.1 cm^{-1}. The average difference between the observed and Ritz wavelengths, calculated from the literature values of the level energies, is 0.03 nm. Using the optimized energies from the procedure above and excluding lines from levels defined by a single transition, a similar average of 0.02 nm is found. While the uncertainties of the level energies for the Au II optimization are larger than those of Au, the agreement between the literature values and the optimized energies is good. On average, the difference between these energies is 2.8 cm^{-1}, which corresponds to a wavelength uncertainty of $\pm$0.04 nm at 400 nm.

In many cases, expected transitions of Au III are coincident in wavelength with peaks in the spectra. Two peaks are possibly the known Au III transitions at 208.28 (Au II blend) and 322.8 nm from Iglesias (1960). It was explicitly stated by RW that no Au III emission was present in their Fourier transform spectra, and only very weak lines in the UV were observed in their grating spectra. They asserted that this may be explained by charge state loss via charge exchange with the helium gas in their hollow cathode. Alternatively, it is possible that collisional de-excitation limited their detections to the strongest transitions in the UV for many of their levels. Given the possible Au III in our spectra, the high temperature ($\sim$10 eV), and the low pressure compared to hollow cathodes operating at several mTorr, the intensities and level assignments of the observed lines may be attributed to significantly different level populations compared to Rosberg & Wyart (1997). In this work, it is expected that the collisional de-excitation is reduced and thus visible transitions from the same levels were observable. The small degree of collisional de-excitation for a complex system like Au in the CTH is consistent with modeling work on Mo by Johnson et al. (2019a).

Almost half of the observed transitions of Au II are at wavelengths longer than 300 nm, and 38 of the previously unobserved transitions are in this region. This is in stark contrast to previous work, which focused shortward of 300 nm. These 38 transitions stem from the $5d^9(nl = 6d, 6p, 7p, 7s, 8s)$ levels at primarily high energies ($E > 100{,}000\ cm^{-1}$).

The 51 newly observed transitions are spread over a large number of upper levels. Five originate from the $J = 2$ and 3 fine structure levels in the $5d^97s$ and $5d^98s$ configurations. Seven transitions connect the $5d^96p$ and $5d^97p$ configurations to the $5d^86s^2$ and $5d^96d$ configurations. Thirty transitions connect the $5d^96d$ levels to four of the $5d^96p$ and 26 of the $5d^86s6p$ fine structure levels. We note that these two-electron transitions, $5d^96d \rightarrow 5d^86s6p$, are forbidden under normal *LS* coupling but may be allowed in Au II, as the configuration interaction is nonnegligible (see the calculations of Rosberg & Wyart 1997). Just as in Au I, the two-electron transitions are often similar in intensity to one-electron transitions during current-driven plasmas. Lastly, nine transitions connect the $5d^86s6p$ levels to low-lying levels in the $5d^86s^2$ configuration. These transitions, $5d^86s6p \rightarrow 5d^86s^2$, are extremely common in RW's grating spectra, where over 70% of their transitions involve a $5d^86s6p$ level.

It is not unexpected that the majority of the newly observed lines are between levels with different core configurations. Transitions of this type, e.g., $5d^7(...) \rightarrow 5d^8(...)$ or $5d^8(...) \rightarrow 5d^9(...)$, constitute $\sim$50% of the lines in RW's grating spectra. Lines of this nature are generally absent from the current-free portion of the discharge and typically strong during current-driven portions. Presence during only the hottest portions of the discharge is consistent with the energies of the upper levels and lends confidence to the assignments of the levels in these transitions.

4. Conclusion

We undertook a systematic study of the Au I and Au II systems by studying spectra from eroding a gold-plated target inside the CTH experiment at Auburn University. The unique set of plasma conditions in the CTH allows for significant excitation of the levels of interest. The use of both gold- and nickel-plated probe tips makes it possible to isolate emission lines unique to the surface plating of the probe tips. The procedure developed is applicable to a wide variety of elements. For elements that are not plate-able, targets of pure metal may be used, as was the case in Johnson et al. (2019b). Collisional-radiative modeling of Fe II emission suggests that plasma conditions at the probe tips ($T_e \sim 10$ eV, $n_e \sim 10^{12}$ cm^{-3}) are comparable to those found in previous experiments at the CTH (Johnson et al. 2019b). The spectra suggest the presence of some Au III emission.

Eighty-six unique emission lines attributed to Au I are observed, 43 of which were previously unobserved. In Au, 18 $5d^96s6p$ levels are identified, and all but two of the $5d^96s6d$ levels proposed by Platt & Sawyer (1941) and Ehrhardt & Davis (1971) are observed. In Au II, 76 unique lines were found, 51 of which were previously unobserved. Over half of the newly observed lines from Au II are in the visible longward of 300 nm. The line classifications in both systems are corroborated by a least-squares level optimization, and the resulting level energies and their uncertainties are consistent with the resolution of the spectrometer.

Using the peaks within the overlaps of neighboring wavelength windows, observed intensities are placed on the same relative scale. For both Au I and II, two-electron transitions between levels with different core configurations are found and are similar in intensity to LS-allowed one-electron transitions. Compared to previous work, which primarily focused on UV transitions, the CTH experiments revealed new emission lines in both the UV and visible spectra. When combined with the previous line surveys of Platt & Sawyer (1941), Ehrhardt & Davis (1971), and Rosberg & Wyart (1997), this work provides useful benchmarks for future atomic structure calculations of these systems.

The authors gratefully acknowledge funding support from the Clemson University College of Science, the National Science Foundation (grant Nos. 1815833, 1815932, and 1816984), and the Department of Energy (grant No. DE-FG02-00ER54610). Many thanks are extended to the staff

operating the Compact Toroidal Hybrid: James Kring, Kevin Ross, Nic Allen, and Ellie Williamson.

Software: ColRadPy (Johnson et al. 2019a), LOPT (Kramida 2011).

ORCID iDs

S. J. Bromley https://orcid.org/0000-0003-2110-8152
C. A. Johnson https://orcid.org/0000-0002-5640-5854
G. J. Hartwell https://orcid.org/0000-0002-2855-2304
S. D. Loch https://orcid.org/0000-0002-3822-6756
P. C. Stancil https://orcid.org/0000-0003-4661-6735
B. M. McLaughlin https://orcid.org/0000-0002-5917-0763
C. E. Sosolik https://orcid.org/0000-0001-6686-2584
J. P. Marler https://orcid.org/0000-0002-1626-5615

References

Abbott, B. P., Abbott, R., Abbott, T. D., Acernese, F., & Ackley, K. 2017, PhRvL, 119, 161101
Brown, C. M., & Ginter, M. L. 1978, JOSA, 68, 243
Castelli, F., Cowley, C. R., Ayres, T. R., Catanzaro, G., & Leone, F. 2017, A&A, 601, A119
Côté, B., Fryer, C. L., Belczynski, K., et al. 2018, ApJ, 855, 99
Coulter, D. A., Foley, R. J., Kilpatrick, C. D., et al. 2017, Sci, 358, 1556
Drout, M. R., Piro, A. L., Shappee, B. J., et al. 2017, Sci, 358, 1570
Ehrhardt, J. C., & Davis, S. P. 1971, JOSA, 61, 1342
Fontes, C. J., Fryer, C. L., Hungerford, A. L., Wollaeger, R. T., & Korobkin, O. 2020, MNRAS, 493, 4143
Fuhrmann, K. 1989, A&AS, 77, 345
Guthrie, B. N. G. 1984, MNRAS, 206, 85
Hartwell, G., Knowlton, S., Hanson, J., Ennis, D., & Maurer, D. 2017, Fusion Science and Technology, 72, 76
Iglesias, L. 1960, JRNBA, 64A, 481
Jaschek, M., & Malaroda, S. 1970, Natur, 225, 246
Johnson, C., Loch, S., & Ennis, D. 2019a, Nuclear Materials and Energy, 20, 100579
Johnson, C. A., Ennis, D. A., Loch, S. D., et al. 2019b, PPCF, 61, 095006
Kajino, T., Aoki, W., Balantekin, A., et al. 2019, PrPNP, 107, 109
Kasen, D., Badnell, N. R., & Barnes, J. 2013, ApJ, 774, 25
Kasen, D., Metzger, B., Barnes, J., Quataert, E., & Ramirez-Ruiz, E. 2017, Natur, 551, 80
Kawaguchi, K., Shibata, M., & Tanaka, M. 2018, ApJL, 865, L21
Kramida, A. 2011, CoPhC, 182, 419
Kramida, A. 2019, Atoms, 7, 64
Kramida, A., Ralchenko, Yu., Reader, J. & NIST ASD Team 2020, NIST Atomic Spectra Database v5.7.1 (Gaithersburg, MD: NIST), https://physics.nist.gov/asd
Liccardo, V., Malheiro, M., Hussein, M. S., Carlson, B. V., & Frederico, T. 2018, EPJA, 54, 221
Margutti, R., Berger, E., Fong, W., et al. 2017, ApJL, 848, L20
Morton, D. C. 2000, ApJS, 130, 403
Platt, J. R., & Sawyer, R. A. 1941, PhRv, 60, 866
Quinet, P. 2017, CaJPh, 95, 790
Rosberg, M., & Wyart, J.-F. 1997, PhyS, 55, 690
Whaling, W., Carle, M., & Pitt, M. 1993, JQSRT, 50, 7